

An uncertainty quantification framework for logistic regression based geospatial natural hazard modeling



Weiwei Zhan^{a,b,*}, Laurie G. Baise^b, Babak Moaveni^b

^a Department of Civil, Environmental and Construction Engineering, University of Central Florida, Orlando, FL 32826, USA

^b Department of Civil and Environmental Engineering, Tufts University, Medford, MA 02155, USA

ARTICLE INFO

Keywords:

Liquefaction
Geospatial modeling
Uncertainty
Bayesian inference
Logistic regression
Classification error

ABSTRACT

There is a class of data-driven global natural hazard predictive models that take advantage of broadly available geospatial proxies. These data-driven geospatial models have been commonly used for landslides and are becoming more available in recent years for liquefaction. Logistic regression is the most common method for predicting these ground failure occurrences. These models do not often include robust quantification of uncertainties although they are widely used in the pre-disaster planning and post-disaster response around the world. Taking the logistic regression based global geospatial liquefaction model (GGLM) (Zhu et al., 2017) as an example, we propose an uncertainty quantification (UQ) framework that consists of characterization of different sources of uncertainty, model sensitivity analysis, and forward uncertainty propagation. In this study, we have identified the main sources of uncertainty in such predictive models as parameter estimation uncertainty, modeling error, and geospatial input uncertainty. A Bayesian inference algorithm is used to quantify the posterior distribution of model parameters and quantify model parameter estimation uncertainties which are found to be negligible when a large amount of data is used in the parameter estimation process. Modeling errors are characterized based on the observed residuals between model predictions and measurements and by fitting a Gaussian distribution to the liquefaction probability residuals. The geospatial input uncertainties are characterized using the literature and expert judgment and propagated into model output. Second, we investigate the sensitivity of model output to different uncertain inputs and find that the variance of model output is largely controlled by the geospatial input uncertainties and model errors. Last, we propose an approximate forward uncertainty propagation method, which provides comparable results to a Monte Carlo simulation-based method with better computational efficiency. The proposed UQ framework provides a measure of uncertainty on model predictions and can be applied to any logistic-regression models and other geospatial modeling problems.

1. Introduction

Since 1990, natural hazards have led to over 1.6 million fatalities globally, and the economic losses are estimated at an average of around 260–310 billion USD per year (UNDRR, 2015). With the advancements in remote sensing techniques and geospatial big data, data-driven models play an important role in natural hazard risk management. The scientific, insurance, and policy communities have developed many data-driven models to characterize and map hazard in terms of probability of occurrence at the regional or global scales, using geospatial proxies hereinafter called geospatial natural hazard models (GNHMs). However, uncertainties are pervasive in GNHMs due to the intrinsic variability of natural hazards and geologic processes, missing or

erroneous data, resolution and scale, parameter estimation uncertainty, model-based or structural uncertainty, and knowledge gaps, among other factors (Riley et al., 2016). When these uncertainties propagate into risk models, the uncertainty can have a significant impact; therefore, quantifying and reducing uncertainty in natural hazard modeling are important for risk modeling.

Geospatial natural hazard models can be broadly grouped into physics-based models and data-driven models. Physics-based models use governing equations to describe the physics of natural hazard and model the spatiotemporal evolution of natural hazards, such as earthquake (Taborda and Bielak, 2011), tsunami (Furumura et al., 2011), landslide (Feng et al., 2022), and wildfire (Finney et al., 2011). These physics-based models, once calibrated, can be used to simulate different

* Corresponding author at: 12760 Pegasus Dr, Orlando, FL 32826, USA.

E-mail address: weiwei.zhan@ucf.edu (W. Zhan).

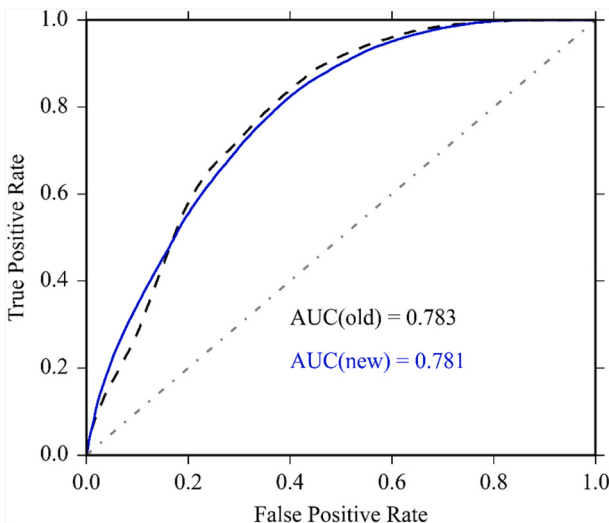


Fig. 1. Receiver Operating Curve of the old GGLM (Zhu et al., 2017) and the new GGLM using all log-transformed explanatory variables as inputs.

hazard scenarios which make them particularly useful in probabilistic risk planning. Many data-driven natural hazard models take advantage of broadly available geospatial proxies and geospatial natural hazard occurrence data and use statistical learning or machine learning to predict natural hazard occurrence (Totschnig and Fuchs, 2013; Eidvigg et al., 2014; Zhu et al., 2015; Zhu et al., 2017; Fan et al., 2018; Lombardo and Mai, 2018; Lin et al., 2021; Lu et al., 2022). Natural hazard occurrence is represented as a binary process, whereas, the geospatial proxies are often continuous variables, and sometimes categorical variables. Despite the lack of physical interpretation for regression-based function form, geospatial natural hazard models can show equivalent or better performance when compared to physics-informed models (e.g., Geyin et al., 2020).

Systematical uncertainty quantification for data-driven natural hazard models has been less explored than physics-based ones. As in introduction to a book on natural hazard uncertainty assessment, Riley et al. (2016) provides a survey of emerging techniques in assessment of uncertainty in natural hazard modeling. As natural hazards can be affected by many factors, sensitivity analysis is useful to identify key factors driving the natural hazard phenomenon and provides insight for model optimization. In the same volume, Thompson and Warmink (2016) provide a general framework for identifying and classifying uncertainties in natural hazard modeling, which highlights the importance of a transparent and systematic identification of uncertainties to guide subsequent modeling and decision processes. More specifically, Ujjwal et al. (2020) provide a cloud-based framework for sensitivity analysis of natural hazards with large-scale wildfire simulations as the use case.

Inspired by UQ frameworks used in scientific computing (Marelli and Sudret, 2014), we aim to provide a general UQ framework for data-driven geospatial natural hazard modeling. The geospatial global liquefaction hazard model (GGLM) developed by Zhu et al. (2017) using logistic regression is used to demonstrate the UQ framework, and the model details are described in Section 2. The UQ framework includes three components: identify and quantify different sources of uncertainty (Section 3), sensitivity analysis showing the main sources that contribute to output variability (Section 4), and forward uncertainty propagation demonstrating how uncertainty affects the probabilistic prediction of the natural hazard (in this case liquefaction) at both site and regional scales (Section 5). The main findings and some implications of the UQ framework on natural hazard modeling are summarized in Section 6.

2. Overview and modifications of the GGLM

Soil liquefaction is one of the secondary hazards caused by earthquake shaking and can cause ground failure and severe structural damages (Tokimatsu et al., 2012; Van Ballegooij et al., 2014). Liquefaction susceptibility is known to be correlated with surficial geology in terms of age and depositional environment (Youd and Perkins, 1978), geomorphology (Matsuoka et al., 2015), and soil saturation as described by distance to river or height above surface water (Zhu et al., 2015). These known correlations provided the basis for developing different geospatial liquefaction hazard models for regional liquefaction susceptibility mapping (e.g., Zhu et al., 2015; Zhu et al., 2017; Kim et al., 2018; Bozzoni et al., 2021; Todorovic and Silva, 2022). Zhu et al. (2015) and Zhu et al. (2017) developed geospatial liquefaction hazard models using geospatial proxies for soil density and soil saturation and integrated earthquake-specific ground shaking intensity measures into geospatial liquefaction hazard modeling. As these ground shaking intensity measures can be estimated quickly after the earthquake occurrence by the United States Geological Survey (USGS) ShakeMap (Worden et al., 2020), this type of geospatial liquefaction hazard model can be used in near-real-time hazard response and loss estimation. The Zhu et al. (2017) geospatial liquefaction hazard models use liquefaction observation data from 27 earthquakes across six countries. One model shows more promising results in coastal regions ("model 1" in Zhu et al., 2017) and another one shows more promising results in noncoastal regions ("model 2" in Zhu et al., 2017). These two models are called global geospatial liquefaction hazard models as they use globally available geospatial proxies as inputs and therefore they can be implemented globally. The noncoastal model in Zhu et al. (2017) has been used as the primary liquefaction model in the USGS near-real-time ground failure product (Allstadt et al., 2022). The overall performance and regional efficacy of the global geospatial liquefaction model are discussed in Rashidian and Baise (2020).

To illustrate the proposed UQ framework, this study will quantify uncertainty of the primary global geospatial liquefaction model (i.e., "model 2" in Zhu et al., 2017), hereinafter termed as GGLM. The GGLM predicts the probability of liquefaction occurrence (i.e., a categorical variable describing the liquefaction surface manifestation) using five geospatial proxies, peak ground velocity (PGV) estimated by the USGS ShakeMap, the averaged shear wave velocity within the top 30 m ground (V_{S30}), mean annual precipitation (*precip*), distance to the nearest water body (*dw*), and ground water table depth (*wtd*). The function form of the GGLM is the widely used logistic function and the model parameters are trained from a liquefaction database collected from 27 earthquakes across six countries (see Eq. 1).

$$f(x) = P(y = 1) = \frac{1}{1 + e^{-Z(x)}}, \quad (1)$$

where $P(y = 1)$ is the probability of liquefaction occurrence; y is the liquefaction observation (1 for liquefaction, 0 for non-liquefaction); $\frac{1}{1 + e^{-Z(x)}}$ is the logistic regression function; x is the vector of explanatory variables (geospatial proxies in geospatial natural hazard models); and Z is a function of explanatory variables. The GGLM uses a linear combination of explanatory variables as shown in Eq. (2).

$$Z(x) = w_0 + w_1 \times \ln(PGV) + w_2 \times \ln(V_{S30}) + w_3 \times \ln(precip) + w_4 \times \ln(dw) + w_5 \times \ln(wtd), \quad (2)$$

where PGV is the peak ground velocity (cm/s); V_{S30} is the time-averaged shear wave velocity to a depth of 30 m, which is estimated using the slope-based V_{S30} model (Wald and Allen, 2007); *precip* is the mean annual precipitation (mm) from the WordClim database (<https://worldclim.org/>); *dw* is the distance to nearest water body (km) computed from the Hydro-SHEDS (<https://www.hydrosheds.org/>); *wtd* is the water

Table 1

Parameter estimation uncertainty of the geospatial liquefaction hazard model.

Coefficients	Intercept	$w_{\ln(\text{PGV})}$	$w_{\ln(V_{S30})}$	$w_{\ln(\text{precip})}$	$w_{\ln(dw)}$	$w_{\ln(wtd)}$
Mean	6.731	0.279	-1.459	0.167	-0.695	-0.130
Std	0.067	0.003	0.013	0.004	0.004	0.003
COV (%)	1.0	1.0	-0.9	2.6	-0.6	-2.6

Table 2

Correlation matrix for the model parameters of the geospatial liquefaction hazard model.

Correlation	Intercept	$w_{\ln(\text{PGV})}$	$w_{\ln(V_{S30})}$	$w_{\ln(\text{precip})}$	$w_{\ln(dw)}$	$w_{\ln(wtd)}$
Intercept	1.00	-0.02	-0.88	-0.24	0.11	0.70
$w_{\ln(\text{PGV})}$		1.00	-0.14	0.08	-0.06	0.09
$w_{\ln(V_{S30})}$			1.00	-0.23	-0.14	-0.80
$w_{\ln(\text{precip})}$				1.00	-0.01	0.16
$w_{\ln(dw)}$					1.00	0.06
$w_{\ln(wtd)}$						1.00

table depth extracted from the global water table depth map (m) (Fan et al., 2013); and w_0, w_1, \dots, w_5 are the regression coefficients.

In order to facilitate the application of the UQ framework, we apply log-transformation to all geospatial explanatory variables, instead of only transforming PGV and V_{S30} (see Table 3 in Zhu et al., 2017) and reoptimize the regression coefficients. The consistent variable transformations are beneficial for the Bayesian inference and forward uncertainty propagation as it results in similar magnitude and a common distribution. The variable transformations do not significantly affect the model classification accuracy as demonstrated by the area under receiver operating characteristic curve (AUC) of models in Fig. 1. The Brier score of the updated GGLM is 0.181 instead of 0.167 in Zhu et al. (2017).

3. Uncertainty quantification for GGLM

Geospatial natural hazard models intrinsically involve different types of uncertainties. In this framework, we identify three types of uncertainty sources: parameter estimation uncertainty, modeling errors, and geospatial input uncertainty. In this section, we quantify (1) estimation uncertainty of model parameters through a Bayesian inference framework, (2) modeling error by fitting a distribution to the observed model prediction residuals, and (3) geospatial explanatory variables from past studies or engineering judgment.

3.1. Bayesian inference for quantifying parameter estimation uncertainty

Under the UQ framework, we treat model parameters as random variables and use the Bayes' theorem to estimate the posterior probability distribution of model parameters.

$$p(\mathbf{w}|\mathbf{D}) = \frac{p(\mathbf{D}|\mathbf{w})p(\mathbf{w})}{p(\mathbf{D})} \propto p(\mathbf{D}|\mathbf{w})p(\mathbf{w}), \quad (3)$$

where \mathbf{w} is the vector of model parameters to be estimated; \mathbf{D} is the vector of available data, i.e., paired geospatial inputs X and liquefaction observation y ; $p(\mathbf{w}|\mathbf{D})$ is the posterior distribution of model parameters; $p(\mathbf{D}|\mathbf{w})$ is the likelihood function as shown in Eq. (4); $p(\mathbf{w})$ is the prior probability distribution of the model parameters; and $p(\mathbf{D}) = \int p(\mathbf{D}|\mathbf{w})p(\mathbf{w})d\mathbf{w}$ is the evidence which is a normalization constant so the probability of the parameters sums to one.

$$p(\mathbf{D}|\mathbf{w}) = \prod_{n=1}^N p_n^{y_n} (1-p_n)^{1-y_n}, \quad (4)$$

In Eq. (4), N is the sample size; n is the sample id ranging from 1 to N ; $p_n = \frac{1}{1+e^{-Z(x)}}$ is the liquefaction probability for sample n predicted using

the logistic function; and y_n is the liquefaction observation for sample n ($y_n = 1$ for liquefaction and $y_n = 0$ for nonliquefaction).

As the solution of posterior distribution of model parameters for logistic regression is intractable (Bishop and Nasrabadi, 2006), we use the Laplace approximation method to estimate $p(\mathbf{w}|\mathbf{D})$. Laplace approximation aims to find a Gaussian approximation to the posterior probability density defined over a set of continuous variables (Bishop and Nasrabadi, 2006). We assume a Gaussian distribution for the model parameter prior with the general form as shown in Eq. (5).

$$p(\mathbf{w}) = N(\mathbf{w}|\mathbf{m}_0, \mathbf{S}_0) \quad (5)$$

where \mathbf{m}_0 and \mathbf{S}_0 are the mean vector and covariance matrix of the model parameters, respectively.

Taking the log of both sides in Eq. (3), and substituting Eq. (4) for the likelihood function, and Eq. (5) for the prior distribution, we obtain the posterior distribution (Bishop and Nasrabadi, 2006):

$$\begin{aligned} \ln p(\mathbf{w}|\mathbf{D}) = & -\frac{1}{2}(\mathbf{w} - \mathbf{m}_0)^T \mathbf{S}_0^{-1} (\mathbf{w} - \mathbf{m}_0) + \sum_{n=1}^N \{y_n \ln p_n + (1-y_n) \ln(1-p_n)\} \\ & + \text{constant}, \end{aligned} \quad (6)$$

To obtain a Gaussian approximation for the posterior distribution, we first find the maximum-a-posteriori (MAP) estimate \mathbf{w}_{MAP} as the maximum of Eq. 6, which defines the mean of the posterior distribution. The covariance matrix is then estimated as the inverse of the Hessian (second derivative) of the negative log likelihood, which takes the form

$$\mathbf{S}_N = -\nabla \nabla \ln p(\mathbf{w}|\mathbf{D}) = \mathbf{S}_0^{-1} + \sum_{n=1}^N p_n(1-p_n) \mathbf{x}_n \mathbf{x}_n^T, \quad (7)$$

The Gaussian approximation to the posterior distribution therefore takes the form

$$q(\mathbf{w}) = N(\mathbf{w}|\mathbf{w}_{\text{MAP}}, \mathbf{S}_N), \quad (8)$$

The prior distribution uses zero means for all the model parameters, and standard deviation of 100. In that way, the prior distribution is flat, which indicates an uninformative prior distribution. The Laplace approximation is then used to estimate the joint posterior distribution of model parameters. The pairwise correlations between model parameters are estimated using the \mathbf{S}_N by converting the covariance matrix to correlation matrix.

The mean, standard deviation, and coefficient of variation (COV) of the GGLM model parameters are summarized in Table 1. The model parameters show small estimation uncertainty, with the maximum absolute value of COV being 2.6% (for $\ln(\text{precip})$ and $\ln(wtd)$), not exceeding 1.0% for the remaining model parameters. The pairwise correlations between the model parameters of GGLM are shown in Table 2. Two model parameters ($\ln(V_{S30})$ and $\ln(wtd)$) have strong correlations with intercept, and $\ln(V_{S30})$ also shows a strong negative correlation with $\ln(wtd)$. The positive parameter correlation means the model parameter tends to increase with the increase of another model parameter, and vice versa (Li and Vu, 2013). Statistically, the maximum likelihood fitting (Eq. 4) cannot guarantee unique parameter estimation, due to correlations among the parameters. The correlation can be explained by the physical background of liquefaction phenomena. For instance, the site stiffness (V_{S30}) and water table depth (wtd) can affect the soil liquefaction susceptibility jointly. In short, the Bayesian inference results suggest the GGLM tend to have low parameter estimation uncertainty.

3.2. Residual analyses for quantifying modeling error

3.2.1. Modeling error

Modeling errors are due to imperfections of the simplified statistical models in representing complex natural hazard phenomena and inherent randomness of geophysical processes. For geospatial natural hazard models with continuous outputs (i.e., regression models), such as

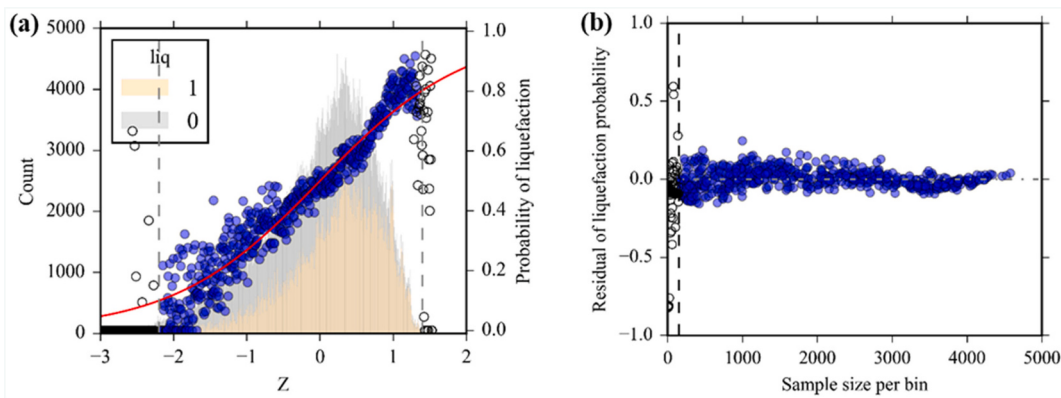


Fig. 2. (a) Comparison between empirical (circles) and theoretical (red curve) liquefaction probabilities. The empty circles indicate bins with sample size <150. The histogram shows the number of liquefaction and non-liquefaction samples. The vertical dashed lines constrain the data range with sufficient sample size for computing empirical liquefaction probability. (b) The correlation between liquefaction probability residuals and sample size per bin. The vertical dashed line indicates sample size for reliable estimation of empirical liquefaction probability. (For interpretation of the references to colour in this figure legend, the reader is referred to the web version of this article.)

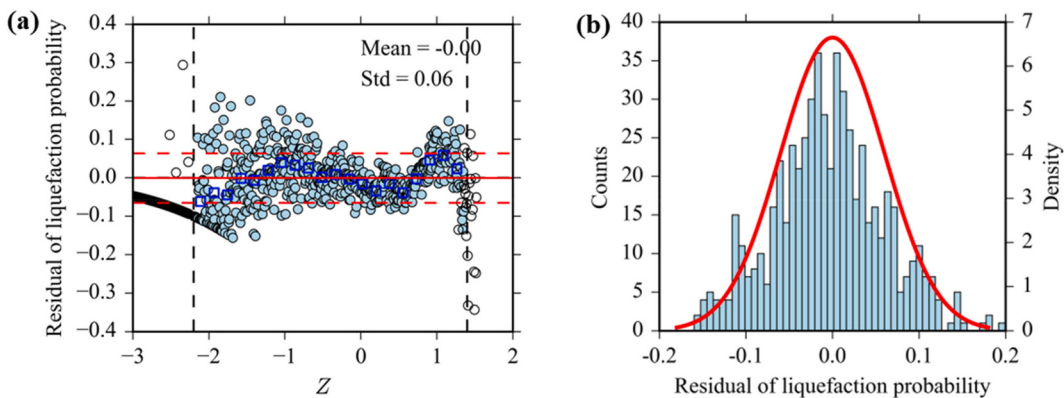


Fig. 3. (a) Relationship between the liquefaction probability residuals and the Z value. The circles with no fill have insufficient samples to estimate empirical liquefaction probability (i.e., the sample size is <150). The blue squares are binned means of liquefaction probability residuals. The red line is the theoretical probability density function for the Gaussian distribution with mean of zero and standard deviation of 0.06. (For interpretation of the references to colour in this figure legend, the reader is referred to the web version of this article.)

Table 3

Proposed mean and modeling error forms of the considered GGLM after the residual analyses.

Stage	Applicable range	$P(y = 1)$	ϵ
1	$Z < -2.2$	0.05	Assumed $N(0, 0.06)^*$
2	$-2.2 \leq Z \leq 1.4$	1 $1 + e^{-Z(x)}$	$N(0, 0.06)$
3	$Z > 1.4$	0.80	Assumed $N(0, 0.06)$

* $N(\mu, \sigma)$ denotes the Gaussian distribution where μ is the mean and σ is the standard deviation.

earthquake ground-motion models (Boore et al., 2014), the modeling errors can be defined as the differences between the observed and predicted hazard intensities. However, for geospatial models with categorical target variables (i.e., classification models), the modeling errors are not easily defined (Liu and Zhang, 2018). Here, we quantify the modeling errors of GGLM in the space of liquefaction probability. Specifically, the model residuals of the GGLM are defined as the differences of empirical and theoretical liquefaction probabilities which are both conditional on the Z value.

$$\epsilon(Z) = P(Z)_{\text{emp}} - P(Z)_{\text{theo}}, \quad (9)$$

where ϵ is the liquefaction probability residual which is considered as

modeling error; $P(Z)_{\text{emp}}$ is the empirical (observed) liquefaction probability which is computed as the ratio of the liquefaction sample size to the total sample size for each Z value bin; and $P(Z)_{\text{theo}}$ is the theoretical (predicted) liquefaction probability which is computed using Eq. (1).

3.2.2. Global residual model

The relationship between the empirical and theoretical liquefaction probabilities is shown in Fig. 2. The empirical liquefaction probabilities are represented for different Z bins based on the corresponding proxies of observed locations, and they match well with the theoretical ones for samples with $Z \in [-2.2, 1.4]$ (i.e., $P(Z)_{\text{theo}} \in [0.1, 0.8]$). It is noted that the observed liquefaction probabilities deviate from the predicted liquefaction probabilities at the low and high Z values, which is likely due to insufficient sample size at these bins for calculating empirical liquefaction probabilities. We use 150 as the threshold sample size per bin to exclude outlier bins based on the relationship between liquefaction probability residuals and the sample size per bin (Fig. 2b).

The liquefaction probability residuals show different patterns at varying Z values (Fig. 3). The GGLM consistently overestimates the liquefaction probability at the very low Z value range ($Z < -2.2$) where the empirical liquefaction probabilities are zero except for a few abnormal high values due to insufficient sample size. At the very-high Z value range ($Z > 1.4$), the model also tends to have a smaller number of reliable estimations of empirical liquefaction probability. For the middle

Table 4

Summary of residual models for different earthquakes.

Earthquake name	Year	Region	Mw	nsamples	Z _{min}	Z _{max}	bias	std
Chiba	1987	Japan	6.5	100,000	-1.5	1.2	-0.03	0.09
Kobe	1995	Japan	6.9	100,000	-1.5	1.5	-0.20	0.14
Tohoku	2011	Japan	9.1	100,000	-1.8	1.5	-0.03	0.11
Niigata1964	1964	Japan	7.6	100,000	-2.2	1.2	-0.07	0.10
Nihonkai	1983	Japan	7.7	100,000	-1.5	1.2	0.02	0.10
Niigata2004	2004	Japan	6.6	100,000	-2.5	1.4	0.02	0.08
Darfield	2010	New Zealand	7.0	100,000	-2	1.2	0.00	0.07
Christchurch	2011	New Zealand	6.1	100,000	-2	1.4	0.03	0.11
Loma Prieta	1989	USA	6.9	79,800	-1.6	1.4	-0.13	0.19
Hokkaido	1993	Japan	7.7	74,200	-2	0.8	0.12	0.09
Chichi	1999	Taiwan	7.6	41,500	-2	1.4	0.00	0.14
Tottori	2000	Japan	6.7	40,600	-1.2	1.4	-0.09	0.17
Pugetsound1965	1965	USA	6.7	12,100	-2.4	1.0	0.12	0.21
Pugetsound1949	1949	USA	6.9	9200	-2.1	1.0	0.07	0.18
Tokachi	2003	Japan	8.3	8100	-1.8	1.2	-0.03	0.22
Wenchuan	2008	China	7.9	6900	-2.8	0.85	0.09	0.25
Miyagi	1978	Japan	7.6	4700	-0.1	1.3	-0.24	0.26
Nisqually	2001	USA	6.8	2900	-1.5	0.6	-0.08	0.31
Northridge	1994	USA	6.6	2200	-2.55	0.4	0.13	0.31
San Simeon	2003	USA	6.6	1100	-0.37	0.25	-0.07	0.39

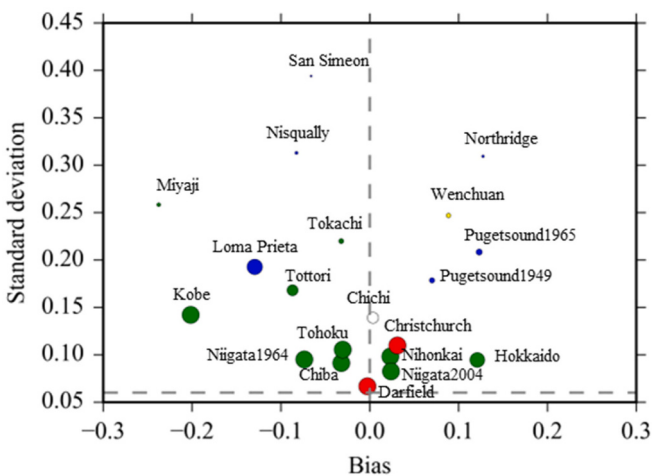


Fig. 4. Summary of liquefaction probability residuals for different earthquakes. The size of circles indicates the sample size per earthquake. The colors indicate different regions. The dashed lines indicate the bias and standard deviation of liquefaction probability residuals for the global dataset.

Z value range ($Z \in [-2.2, 1.4]$), the liquefaction probability residuals have slightly higher variability for negative Z values than for positive values but generally follow a Gaussian distribution as shown in Fig. 3b. In this study, we represent the liquefaction probability residuals as a Gaussian distribution with mean of zero (as the fitting process is unbiased) and standard deviation of 0.06 (Fig. 3b). Based on the residual analyses, we propose conditional mean and residual models for global application of the GGLM (Table 3) which is basically a truncated Gaussian distribution model. For locations with Z between -2.2 to $+1.4$, mean estimate of liquefaction probability is the direct output of the logistic regression model (see Eqs. 1 and 2) while modeling error is represented by the fitted Gaussian distribution in Fig. 3b. For locations with $Z < -2.2$, we recompute the empirical liquefaction probability as the ratio of the number of the liquefaction samples with $Z < -2.2$ to the total number of samples with $Z < -2.2$, and assign this empirical probability value (i.e., 0.05) as the mean estimate of liquefaction probability with $Z < -2.2$. For locations with $Z > 1.4$, we assign the mean estimate of liquefaction probability as 0.8 using the similar method but removing the samples from several outlier Z bins. We assume the residual models for the locations with insufficient samples (i.e., $Z < -2.2$ and $Z > 1.4$) fit the same Gaussian distribution calibrated using the main part of dataset (Fig. 3b) although we do not have enough reliable data to calibrate them. It is noted that our residual analyses also contribute to cap the predicted liquefaction probability.

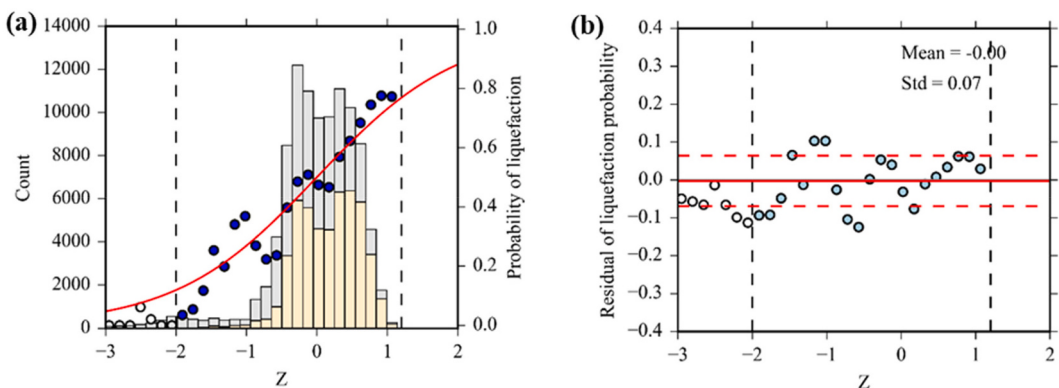


Fig. 5. Liquefaction probability residual model for the 2010 Darfield Earthquake: (a) comparison between empirical and theoretical liquefaction probabilities; and (b) relationship between liquefaction probability residuals and Z values. Empty circles indicate data with insufficient sample for estimating empirical liquefaction probability.

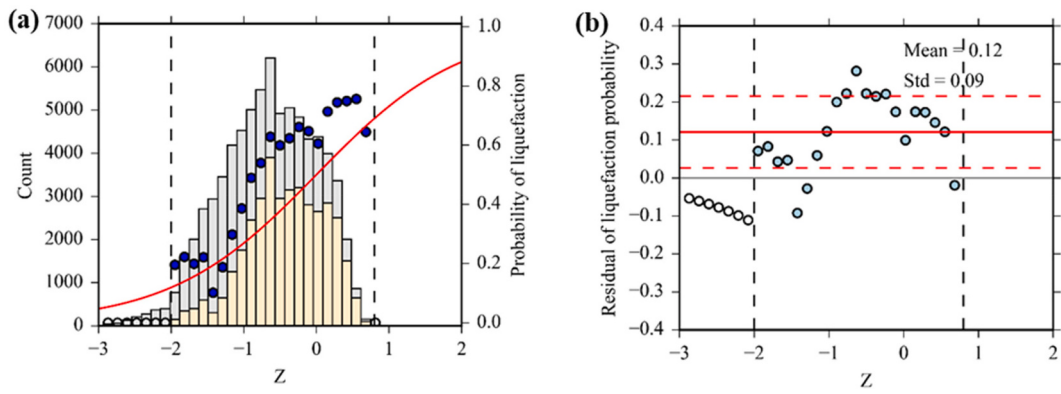


Fig. 6. Liquefaction probability residual model for the 1993 Hokkaido Earthquake: (a) comparison between empirical and theoretical liquefaction probabilities; and (b) relationship between liquefaction probability residuals and Z values. Empty circles indicate data with insufficient sample for estimating empirical liquefaction probability.

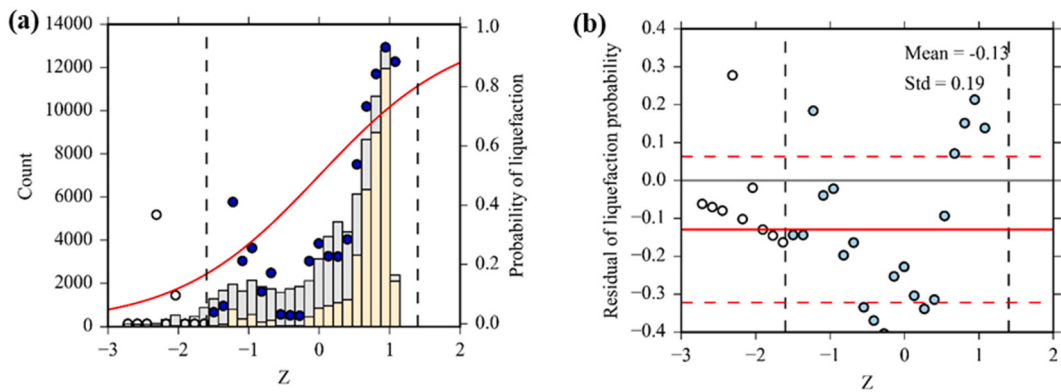


Fig. 7. Liquefaction probability residual model for the 1989 Loma Prieta Earthquake: (a) comparison between empirical and theoretical liquefaction probabilities; and (b) relationship between liquefaction probability residuals and Z values. Empty circles indicate data with insufficient sample for estimating empirical liquefaction probability.

Table 5
Summary of geospatial input uncertainties.

Input	Standard deviation	Reference
$\ln(\text{PGV})$	Grid-specific	USGS ShakeMap
$\ln(V_{S30})$	0.2 for slopes <0.0022 , otherwise 0.43	Seyhan and Stewart, 2014
$\ln(\text{precip})$	Assumed 0.4	This study
$\ln(dw)$	Assumed 0	This study
$\ln(wtd)$	Assumed 0.4	This study

3.2.3. Earthquake-specific residual models

The GGLM is developed using liquefaction data from worldwide earthquakes. Zhu et al. (2017) evaluate the regional difference of the model performance using the AUC for different earthquakes. Here, we investigate the regional difference of GGLM performance using the residual analysis with earthquake-specific datasets. The earthquake-specific liquefaction probability residual models are summarized in Table 4. The Z_{\min} and Z_{\max} show the usable minimum and maximum Z values, respectively, which are decided based on the figures comparing the empirical and theoretical liquefaction probabilities (available in the electronic supplement to this paper). The bias is the mean value of fitted Gaussian distribution to the event specific residuals, indicating the overall offset of liquefaction probability estimation for that event. The standard deviation (std) indicates the variability of liquefaction probability residuals around their mean values.

The bias and variability of earthquake-specific liquefaction probability residuals are shown in Fig. 4. According to Fig. 4, earthquakes with a large number of samples used in training tend to have lower bias and

variability. Most of these earthquakes occurred in data-rich regions, such as Japan, New Zealand, and Taiwan. The model was best-performing for the 2010 Darfield earthquake, with zero bias and a standard deviation of 0.07 as shown in Fig. 5, which are similar to the statistics on the global dataset. The 1993 Hokkaido earthquake has small variability (0.09) while showing a large positive bias (0.12) as shown in Fig. 6, which indicates the GGLM underestimates liquefaction probability at this earthquake. The 1989 Loma Prieta Earthquake shows large negative bias (-0.13) and variability (0.19) as shown in Fig. 7, related to severe overestimation of liquefaction probability at the middle Z value range. It is noted that many of the earthquake-specific residual models involve large uncertainty as those earthquakes with low numbers of samples generally lead to large residuals. This residual analysis provides a quantitative way to evaluate model performance and provide insight for modeling errors for specific earthquakes.

3.3. Geospatial Input uncertainty

Geospatial inputs for the liquefaction model are extracted from geospatial proxy maps. Geospatial proxies are derived from a mix of observations and empirical or physics-based models; and have varying levels of detail about their uncertainty. In this work, we assume all geospatial proxies used in the GGLM are random variables following lognormal distribution, which is widely assumed for the non-negative engineering parameters. The log-transformed geospatial proxies fit the Gaussian distribution with mean values from the corresponding geospatial proxy maps and standard deviation values from Table 5. PGV is the only geospatial proxy used in this study that has reported

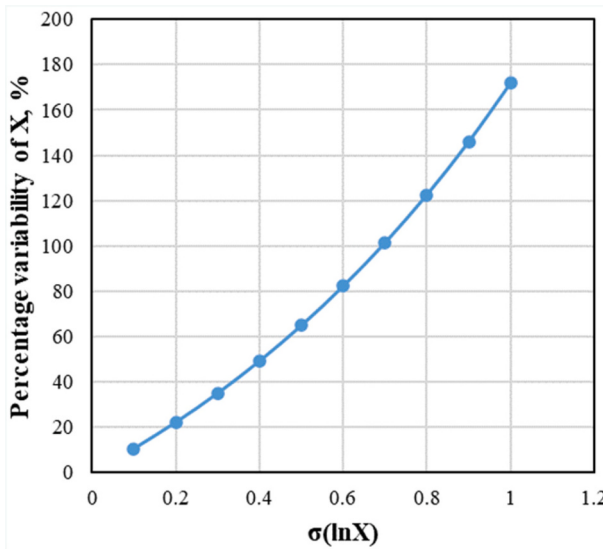


Fig. 8. Illustrative guide on how to interpret the standard deviation of log-transformed variables. This curve shows the percentage variability in the original variable (vertical axis) at the 68% confidence interval for the log-transformed variable with different standard deviations (horizontal axis).

uncertainty in map form (i.e., grid specific). The standard deviation of $\ln(\text{PGV})$ is originally from the residual analyses of ground-motion modeling and directly provided by the ShakeMap (Worden et al., 2020). For the remaining geospatial inputs, we make assumptions about their uncertainty. The standard deviation of $\ln(V_{S30})$ is assigned based on the study of Seyhan and Stewart (2014) which suggest the standard deviations of $\ln(V_{S30})$ are 0.2 for the grids with slope gradient <0.0022 , and 0.4 elsewhere. The standard deviations of $\ln(\text{precip})$ and $\ln(\text{wtd})$ are assumed to be 0.4 based on a conservative interpretation of the source documents (Hijmans et al., 2005; Fan et al., 2013). The standard deviation of $\ln(dw)$ is assumed to be zero, i.e., considered as deterministic. Further studies are warranted to improve these assumptions of geospatial input uncertainty. Interpreting the standard deviation of log-transformed variables is not straightforward as it requires understanding how the logarithmic transformation affects the data and how the standard deviation measures the variability within that transformed data. Here we use the confidence interval method to interpret the standard derivation of log-transformed variables. We compute the percentage change in the original variable corresponding to the increase or decrease of one standard deviation to the log-transformed variable with different standard deviations. Given that 68% of the values fall within one standard deviation of the mean for random variables with Gaussian distribution (i.e., log-transformed variables in this study), the

Table 7

Input for the forward uncertainty propagation analyses at the two demonstration grids.

ID	Grid 1	Grid 2
Observation	Non-liquefaction	Liquefaction
Longitude (°)	-121.7950	-122.3122
Latitude (°)	36.8600	37.7793
elevation (m)	13.4	0.0
slope (°)	0.0181	0.0001
PGV (cm/s)	35.0	28.9
V_{S30} (m/s)	355.6	181.7
precip (mm)	501.5	492.3
dw (km)	1.7	0.0
wtd (m)	12.9	0.1
$\sigma_{\ln(\text{PGV})}$	0.44	0.35
$\sigma_{\ln(V_{S30})}$	0.43	0.20
$\sigma_{\ln(\text{precip})}$	0.40	0.40
$\sigma_{\ln(dw)}$	0.00	0.00
$\sigma_{\ln(wtd)}$	0.40	0.40

Note: numbers in italic fonts are generic values assumed for all grids.

abovementioned percentage change indicate the percentage variability of original variables at the 68% confidence interval. The percentae variability of original variables corresponding to log-transformed variables with different standard derivations are shown in Fig. 8. For instance, $\ln(\text{precip})$ has one standard deviation of 0.4 indicating precip has 49% percentage variability (i.e., could vary from 51% to 149% from the reported value) at the 68% confidence interval.

4. Sensitivity analysis for GGLM

The model sensitivity analysis aims to identify the relative contributions of different sources of uncertainty to the model output variability. This step can guide the forward uncertainty propagation presented in Section 5 and future model optimization.

4.1. Global sensitivity analysis method

Global sensitivity analysis (GSA) can determine how the uncertainty (variance) in the output of a model can be apportioned to different sources of uncertainty in the model input (Saltelli et al., 2005). The uncertainty sources with a small percentage can be fixed to any value within their range (Saltelli et al., 2005). Here we employ the analysis of variance (ANOVA) method through Sobol decomposition to investigate the sensitivity of GGLM to the three sources of uncertainty quantified in the previous section. According to Marelli et al. (2022), the target function is decomposed following Eq. (10) for the purpose of variance decomposition.

Table 6

Summary of the twelve input variables for the global sensitivity analysis.

Group	Variable	Distribution*	Sobol index	Sum†
Parameter estimation uncertainty	Intercept	$N(6.731, 0.067)$	0.005	0.01
	$W_{\ln(\text{PGV})}$	$N(0.279, 0.003)$	0.000	
	$W_{\ln(V_{S30})}$	$N(-1.459, 0.013)$	0.007	
	$W_{\ln(\text{precip})}$	$N(0.167, 0.004)$	0.001	
	$W_{\ln(dw)}$	$N(-0.695, 0.004)$	0.000	
	$W_{\ln(wtd)}$	$N(-0.130, 0.003)$	0.000	
Modeling error	ϵ	$N(0, 0.060)$	0.100	0.10
	$\ln(\text{PGV})$	$N(2.672, 1.782)$	0.295	0.89
	$\ln(V_{S30})$	$N(5.724, 0.375)$	0.355	
	$\ln(\text{precip})$	$N(6.922, 0.617)$	0.013	
	$\ln(dw)$	$N(0.928, 0.591)$	0.201	
Geospatial input uncertainty	$\ln(wtd)$	$N(1.525, 1.427)$	0.041	

* $N(\mu, \sigma)$ denotes the Gaussian distribution where μ is the mean and σ is the standard deviation. .

† Is the ratio of the sum of Sobol' indices for variables belonging to the same group to the sum of Sobol' indices for all random variables.

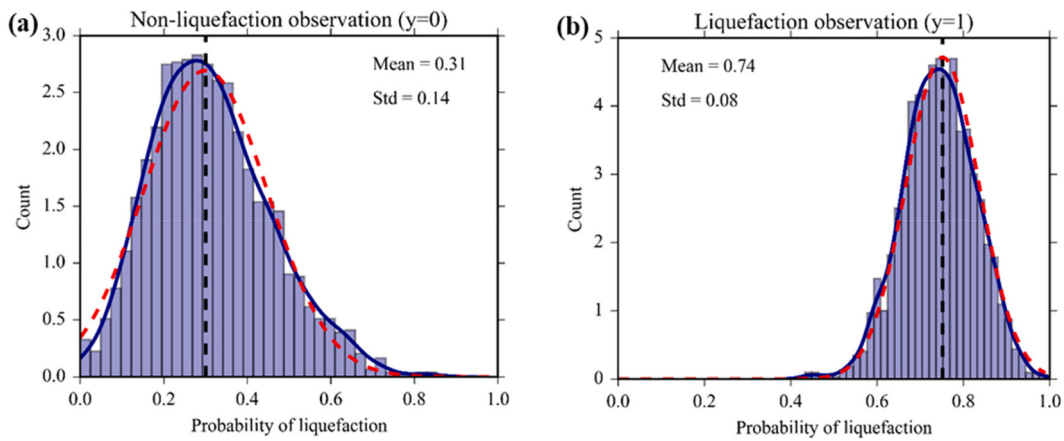


Fig. 9. Forward uncertainty propagation results for the two demonstration grids: (a) non-liquefaction grid; and (b) liquefaction grid. The blue solid curve is the probability density function derived from the histogram of the Monte Carlo Simulation method. The red dashed curve is the Gaussian distribution function of the first-order approximation method. The black dashed line is the result of the standard logistic regression. (For interpretation of the references to colour in this figure legend, the reader is referred to the web version of this article.)

$$f(\mathbf{x}) = f_0 + \sum_{i=1}^M f_i(x_i) + \sum_{1 \leq i < j \leq M} f_{ij}(x_i, x_j) + \dots + f_{1,2,\dots,M}(x_1, \dots, x_M), \quad (10)$$

where $f(\mathbf{x})$ is the target function that can be an arbitrary model (it is the close-form logit function in this work); \mathbf{x} is the vector of input variables, i.e., $\{x_1, \dots, x_M\}$; f_0 is a constant that equals to the expected value of $f(\mathbf{x})$; the first-order and second-order summands (i.e., subset functions in Eq. 10) are defined in Eqs. (11) and (12). The higher-order summands can be constructed in an analogous way.

$$f_i(x_i) = \int_0^1 \dots \int_0^1 f(\mathbf{x}) d\mathbf{x}_{\sim i} - f_0, \quad (11)$$

$$f_{ij}(x_i, x_j) = \int_0^1 \dots \int_0^1 f(\mathbf{x}) d\mathbf{x}_{\sim(ij)} - f_0 - f_i(x_i) - f_j(x_j), \quad (12)$$

where the notation \sim indicates that variables are excluded, e.g., $\mathbf{x}_{\sim i} = \{x_1, \dots, x_{i-1}, x_{i+1}, \dots, x_M\}$.

The total variance of $f(\mathbf{x})$ is defined as:

$$D = \int f^2(\mathbf{x}) d\mathbf{x} - f_0^2, \quad (13)$$

The partial variances are computed as

$$D_{i_1, \dots, i_s} = \int_0^1 \dots \int_0^1 f_{i_1, \dots, i_s}^2(x_{i_1}, \dots, x_{i_s}) dx_{i_1} \dots dx_{i_s}, \quad (14)$$

where $1 \leq i_1 < \dots < i_s \leq M$; $s = 1, \dots, M$. The partial variances have the property that they sum up to the total variance.

The sensitivity measures, called Sobol' indices, are naturally defined based on the above variance decomposition results.

$$S_{i_1, \dots, i_s} = \frac{D_{i_1, \dots, i_s}}{D}, \quad (15)$$

which represent the relative contribution of each group of variables $\{x_{i_1}, \dots, x_{i_s}\}$ to the total variance. The index with respect to one input variable is called the first-order Sobol' index and represents the effects of x_i alone. Multiple-term indices are referred to as higher-order Sobol' indices and account for the interaction effects. The total Sobol's index of input variable x_i , denoted as S_i^T , is the sum of all the Sobol' indices involving the variable x_i .

$$S_i^T = \sum_{\{i_1, \dots, i_s\} \ni i} S_{i_1, \dots, i_s}, \quad (16)$$

For the sensitivity analysis of the GGLM, we use the modified logistic

regression function that adds the model residual to the raw logistic regression function (Eq. 17). We consider twelve input variables belonging to the three groups of uncertainty sources. The distributions of these variables are summarized in Table 6. In this table, the model parameters follow Gaussian distribution with parameters estimated by the Bayesian inference (Table 1). Modeling error is described using the Gaussian distribution with parameters decided by the model residual analysis (Section 3.2). The distribution of geospatial input variables for the sensitivity analysis uses the Gaussian distribution with the mean and standard deviation values determined by dataset (Table 6). The rational for these settings is that we want to evaluate the model sensitivity to the whole applicable range of input space determined by the whole dataset. The Sobol' indices described in Eqs. (16) are computed using Monte Carlo method, as implemented in the UQLab (Marelli and Sudret, 2014).

$$\bar{P}(y=1) = P(y=1) + \epsilon = \frac{1}{1 + e^{-Z(\mathbf{x})}} + \epsilon, \quad (17)$$

where $\bar{P}(y=1)$ is the final liquefaction probability that combines the logistic regression estimation and liquefaction probability residual; $P(y=1)$ is the liquefaction probability estimated by the logistic regression model; $Z(\mathbf{x})$ is a linear combination of explanatory variables as shown in Eq. (2); and ϵ is the liquefaction probability residual as shown in Eq. (9).

4.2. Global sensitivity analysis results

The global sensitivity analysis results for the GGLM considering twelve uncertain inputs are summarized in Table 6. The parameter estimation uncertainty for the GGLM is negligible as it accounts for only 1% of the total variance. The model errors explain 10% of the total variance, and the input variables explain 89% of the total variance. Within the group of input variables, $\ln(V_{S30})$ and $\ln(PGV)$ show dominant contributions (which explain 65% of the total variance), followed by $\ln(dw)$ (which explain 20% of the total variance). The other two saturation parameters show small contribution to the total variance, which implies that they are less important features in the GGLM (Hussain, 2008). It is noted that modeling error may contribute more in some regions as the earthquake specific model residuals tend to have larger variability (and bias) than the global residual model used here.

5. Uncertainty propagation for GGLM

The last step of the UQ framework aims to provide an application of the prior uncertainty quantification results to the prediction of the natural hazard occurrence through uncertainty propagation. Using

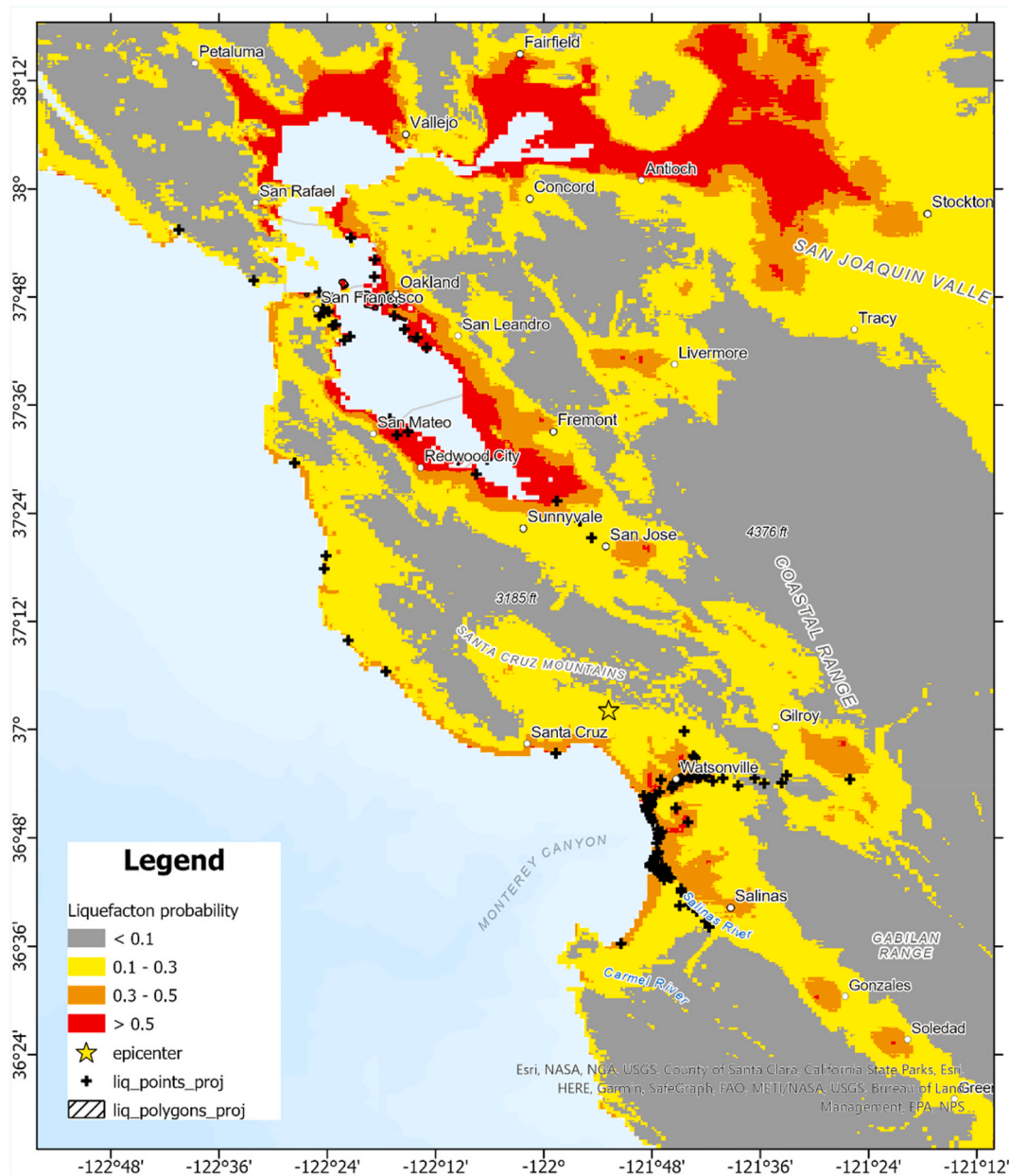


Fig. 10. Mean value of liquefaction probability in the 1989 Mw 6.9 Loma Prieta Earthquake (California, USA).

forward uncertainty propagation, site-specific and event-specific uncertainty of different variables can be propagated into the model output. The resulting probabilistic outputs can provide more information for decision making and risk communication. This section introduces two uncertainty propagation methods: Monte Carlo Simulation and an approximation method, followed by demonstration calculations at grid and region levels for the GGLM.

5.1. Uncertainty propagation methods

Forward uncertainty propagation aims to investigate the effects of uncertainty sources on the uncertainty of model prediction. We ignore parameter estimation uncertainties as their contribution on the variability of model outputs are negligible as demonstrated in Section 4 and summarized in Table 6. Here, we employ two methods to propagate modeling errors and geospatial input uncertainties to the prediction of liquefaction probability. The first method is the Monte Carlo Simulation (MCS) method, in which we independently generate 2000 samples of

model errors and geospatial inputs based on their probability distributions and compute 2000 predictions using Eq. (17). The second method is a first-order approximation method that aims to mitigate the expensive computational cost of MCS method in regional applications of geospatial natural hazard mapping.

To develop the first-order approximation for the forward uncertainty propagation, we assume geospatial proxies (x) are independent Gaussian random variables, such that Z is a Gaussian random variable, and its mean and standard deviation are computed following Eqs. (18) and (19).

$$\mu_Z = w_0 + w_1 \times \mu_{ln(PGV)} + w_2 \times \mu_{ln(Vs30)} + w_3 \times \mu_{ln(precip)} + w_4 \times \mu_{ln(dw)} + w_5 \times \mu_{ln(wtd)}, \quad (18)$$

$$\sigma_Z^2 = w_1^2 \times \sigma_{ln(PGV)}^2 + w_2^2 \times \sigma_{ln(Vs30)}^2 + w_3^2 \times \sigma_{ln(precip)}^2 + w_4^2 \times \sigma_{ln(dw)}^2 + w_5^2 \times \sigma_{ln(wtd)}^2, \quad (19)$$

As a result, the liquefaction probability estimated by the logistic

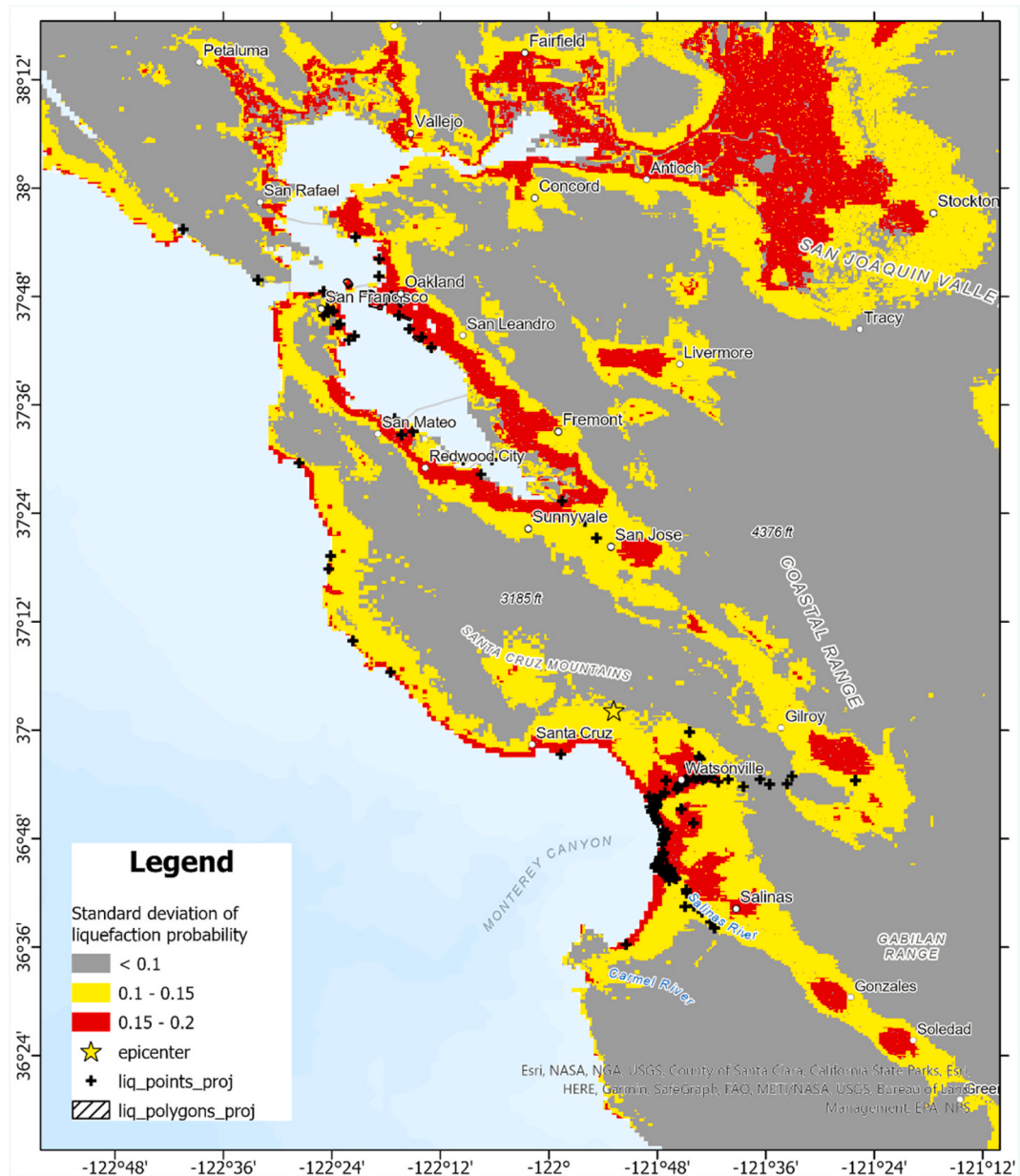


Fig. 11. Standard deviation of liquefaction probability in the 1989 Mw 6.9 Loma Prieta Earthquake (California, USA) based on the approximation method for forward uncertainty propagation.

model is also a Gaussian random variable, and its mean and standard deviation as described in Eqs. (20) and (21):

$$\mu_P = \frac{1}{1 + e^{-\mu_Z}}, \quad (20)$$

$$\sigma_P = \sigma_Z \times \mu_P \times (1 - \mu_P), \quad (21)$$

Then, we assume \bar{P} and e are independent Gaussian random variables, resulting in P as a Gaussian random variable with mean and standard deviation as described in Eqs. (22) and (23):

$$\mu_{\bar{P}} = \mu_P + \mu_e, \quad (22)$$

$$\sigma_{\bar{P}} = \sqrt{\sigma_P^2 + \sigma_e^2}, \quad (23)$$

5.2. Grid-level demonstration

To demonstrate and validate the forward uncertainty propagation

for the GGLM, we use two grids in California that experienced the 1989 Mw 6.9 Loma Prieta earthquake. The geospatial proxies of the grids are shown in Table 7. Grids 1 and 2 are labelled as non-liquefaction and liquefaction during this event, respectively. We perform the forward uncertainty propagation for the GGLM using both the MCS and approximation methods. The forward uncertainty propagation results for the two grids are shown in Fig. 9. First, the approximation results (red dashed curves) match well with the MCS results (histograms and blue solid curves), indicating the correctness of the approximation method in propagating the uncertainties. Second, the liquefaction probabilities fit a Gaussian distribution with mean value which matches the model predictions as the modeling error is zero-mean. The standard deviations of liquefaction probabilities can be viewed as the confidence on model predictions and vary from grid to grid and event to event as the geospatial input proxies vary. This example demonstrates (1) the approximation method presented herein has sufficient accuracy for use in regional applications, and (2) how different sources of uncertainty can be propagated practically for model predictions.

5.3. Region-level demonstration

To demonstrate region-level application of the approximation method for forward uncertainty propagation, we use the 1989 Loma Prieta Earthquake. As the MCS is computationally expensive, we use the approximation method for the region-level forward uncertainty propagation application. The forward uncertainty propagation is implemented using raster calculations in the ArcGIS platform. The input maps for mean values of the five input geospatial proxies are directly downloaded from corresponding resources. The input map of the PGV standard deviation is directly downloaded from the USGS' ShakeMap. The input map for the standard deviation of $\ln(V_{S30})$ is generated based on Table 5. The standard deviation for the other four variables ($\ln(\text{precip})$, $\ln(dw)$, $\ln(wtd)$, and ϵ) are included as constants. The mean liquefaction probability map for the 1989 Loma Prieta earthquake is shown in Fig. 10, against the liquefaction observation data (shown as block dots). The map for the standard deviation of liquefaction probability is shown in Fig. 11. The results suggest that the low-liquefaction-probability areas (hills and stiff sites in Fig. 11) have low uncertainty, which implies the geospatial model is confident and consistently accurate when predicting low liquefaction probability. The uncertainty is higher in high-liquefaction-probability areas indicating that there are more misclassifications in high-probability regions at the pixel level. Such probabilistic representations of model predictions will enable better risk communication and including of hazard in risk calculations.

6. Summary and conclusions

Geospatial natural hazard models are widely used in regional hazard and risk assessments. The GGLM used herein is a widely used product in the USGS earthquake event page communication. However, pervasive uncertainty exists in geospatial natural hazard modeling due to natural complexity, model imperfection, and geospatial data quality. This study provides an uncertainty quantification framework for data-driven geospatial liquefaction hazard models, which includes identifying and quantifying different sources of uncertainty, a global sensitivity analysis, and forward uncertainty propagation.

Taking the global geospatial liquefaction hazard model as a demonstration, we quantify the parameter estimation uncertainty using the Bayesian inference. Parameter estimation uncertainty is found to be negligible for the GGLM due to the large dataset used in model development. A novel residual analysis method is proposed to quantify the modeling error in terms of liquefaction probability residuals. A conditional global residual model is proposed to describe the residual trend based on the aggregate analysis of the global dataset. A similar residual analysis is applied to event-specific data and identifies event-specific patterns of model bias and variance. The global sensitivity analyses consider twelve factors belonging to the three uncertainty sources. The results suggest the geospatial input uncertainty contributes most to the model output variability (89%), followed by the modeling error (10%). The contribution of parameter estimation uncertainty is negligible (1%). Three geospatial factors within the group of geospatial input uncertainty, $\ln(V_{S30})$, $\ln(\text{PGV})$, and $\ln(dw)$, show dominant effects on model output (contributing to 85% of the total variance), which implies they should be used as the primary input features for geospatial liquefaction hazard modeling.

We demonstrate a computationally efficient first-order approximation method for forward uncertainty propagation which provides similarly accurate results as compared to MCS forward uncertainty propagation which is significantly more computationally intensive. When applied to the region-scale, the forward uncertainty propagation results in probabilistic estimations of liquefaction occurrence, which could convey additional information about the expected confidence in model outputs as well as risk models and risk communication. In summary, the UQ framework in this paper can provide the expected uncertainty on the model output and can be implemented to different types

and classes of data-driven geospatial natural hazard models.

CRediT authorship contribution statement

Weiwei Zhan: Conceptualization, Formal analysis, Methodology, Writing – original draft. **Laurie G. Baise:** Funding acquisition, Supervision, Validation. **Babak Moaveni:** Supervision, Validation, Writing – review & editing.

Declaration of Competing Interest

Laurie Baise & Babak Moaveni reports financial support was provided by United States Geological Survey.

Data availability

Data will be made available on request.

Acknowledgments

This work was supported under the U.S. Geologic Survey (USGS), Department of the Interior, under USGS Award Number G22AP00048. The work has greatly benefited from discussions with Eric Thompson at USGS. Any use of trade, firm, or product names is for descriptive purposes only and does not imply endorsement by the U.S. Government.

Appendix A. Supplementary data

Supplementary data to this article can be found online at <https://doi.org/10.1016/j.engeo.2023.107271>.

References

- Allstadt, K.E., Thompson, E.M., Jibson, R.W., Wald, D.J., Hearne, M., Hunter, E.J., Fee, J., Schovanc, H., Slosky, D., Haynie, K.L., 2022. The US Geological Survey ground failure product: Near-real-time estimates of earthquake-triggered landslides and liquefaction. *Earthquake Spectra* 38 (1), 5–36.
- Bishop, C.M., Nasrabadi, N.M., 2006. *Pattern Recognition and Machine Learning*. Springer, New York.
- Boore, D.M., Stewart, J.P., Seyhan, E., Atkinson, G.M., 2014. NGA-West2 equations for predicting PGA, PGV, and 5% damped PSA for shallow crustal earthquakes. *Earthquake Spectra* 30 (3), 1057–1085.
- Bozzoni, F., Boni, R., Conca, D., Meisina, C., Lai, C.G., Zuccolo, E., 2021. A geospatial approach for mapping the earthquake-induced liquefaction risk at the European scale. *Geosciences* 11 (1), 32.
- Eidsvig, U.M.K., Papathoma-Köhle, M., Du, J., Glade, T., Vangelsten, B.V., 2014. Quantification of model uncertainty in debris flow vulnerability assessment. *Eng. Geol.* 181, 15–26.
- Fan, Y., Li, H., Miguez-Macho, G., 2013. Global patterns of groundwater table depth. *Science* 339 (6122), 940–943.
- Fan, X., Scaringi, G., Xu, Q., Zhan, W., Dai, L., Li, Y., Pei, X., Yang, Q., Huang, R., 2018. Coseismic landslides triggered by the 8th August 2017 M s 7.0 Jiuzhaigou earthquake (Sichuan, China): factors controlling their spatial distribution and implications for the seismogenic blind fault identification. *Landslides* 15 (5), 967–983.
- Feng, K., Huang, D., Wang, G., Jin, F., Chen, Z., 2022. Physics-based large-deformation analysis of coseismic landslides: a multiscale 3D SEM-MPM framework with application to the Hongshian landslide. *Eng. Geol.* 297, 106487.
- Finney, M.A., McHugh, C.W., Grenfell, I.C., Riley, K.L., Short, K.C., 2011. A simulation of probabilistic wildfire risk components for the continental United States. *Stoch. Environ. Res. Risk Assess.* 25 (7), 973–1000.
- Furumura, T., Imai, K., Maeda, T., 2011. A revised tsunami source model for the 1707 Hoei earthquake and simulation of tsunami inundation of Ryujin Lake, Kyushu, Japan. *J. Geophys. Res. Solid Earth* 116 (B2).
- Geyin, M., Baird, A.J., Maurer, B.W., 2020. Field assessment of liquefaction prediction models based on geotechnical versus geospatial data, with lessons for each. *Earthquake Spectra* 36 (3), 1386–1411.
- Hijmans, R.J., Cameron, S.E., Parra, J.L., Jones, P.G., Jarvis, A., 2005. Very high resolution interpolated climate surfaces for global land areas. *Int. J. Climatol.* 25 (15), 1965–1978.
- Hussain, J.N., 2008. Sensitivity analysis to select the most influential risk factors in a logistic regression model. *J. Qual. Reliab. Eng.* 471607.
- Kim, H.S., Sun, C.G., Cho, H.I., 2018. Geospatial assessment of the post-earthquake hazard of the 2017 Pohang earthquake considering seismic site effects. *ISPRS Int. J. Geo-Inf.* 7 (9), 375.

- Li, P., Vu, Q.D., 2013. Identification of parameter correlations for parameter estimation in dynamic biological models. *BMC Syst. Biol.* 7, 91.
- Lin, A., Wotherspoon, L., Bradley, B., Motha, J., 2021. Evaluation and modification of geospatial liquefaction models using land damage observational data from the 2010–2011 Canterbury Earthquake Sequence. *Eng. Geol.* 287, 106099.
- Liu, D., Zhang, H., 2018. Residuals and diagnostics for ordinal regression models: a surrogate approach. *J. Am. Stat. Assoc.* 113 (522), 845–854.
- Lombardo, L., Mai, P.M., 2018. Presenting logistic regression-based landslide susceptibility results. *Eng. Geol.* 244, 14–24.
- Lu, J., Li, W., Zhan, W., Tie, Y., 2022. Distribution and Mobility of Coseismic Landslides Triggered by the 2018 Hokkaido Earthquake in Japan. *Remote Sens.* 14 (16), 3957.
- Marelli, S., Sudret, B., 2014. UQLab: A framework for uncertainty quantification in Matlab. In: *Vulnerability, Uncertainty, and Risk: Quantification, Mitigation, and Management*. American Society of Civil Engineers.
- Marelli, S., Lamas, C., Konakli, K., Mylonas, C., Wiederkehr, P., Sudret, B., 2022. UQLab User Manual – Sensitivity Analysis, Report UQLab-V2.0-106, Chair of Risk, Safety and Uncertainty Quantification, ETH Zurich, Switzerland.
- Matsuoka, M., Wakamatsu, K., Hashimoto, M., Senna, S., Midorikawa, S., 2015. Evaluation of liquefaction potential for large areas based on geomorphologic classification. *Earthquake Spectra* 31 (4), 2375–2395.
- Rashidian, V., Baise, L.G., 2020. Regional efficacy of a global geospatial liquefaction model. *Eng. Geol.* 272, 105644.
- Riley, K., Thompson, M., Webley, P., Hyde, K.D., 2016. Uncertainty in Natural Hazards, Modeling and Decision Support: An Introduction to this Volume. *Natural Hazard Uncertainty Assessment: Modeling and Decision Support*, pp. 1–8.
- Saltelli, A., Ratto, M., Tarantola, S., Campolongo, F., 2005. Sensitivity analysis for chemical models. *Chem. Rev.* 105 (7), 2811–2827.
- Seyhan, E., Stewart, J.P., 2014. Semi-empirical nonlinear site amplification from NGA-West2 data and simulations. *Earthquake Spectra* 30 (3), 1241–1256.
- Taborda, R., Bielak, J., 2011. Large-scale earthquake simulation: computational seismology and complex engineering systems. *Comput. Sci. Eng.* 13 (4), 14–27.
- Thompson, M., Warmink, J.J., 2016. Natural hazard modeling and uncertainty analysis. In: *Natural Hazard Uncertainty Assessment: Modeling and Decision Support*. John Wiley & Sons, pp. 9–19.
- Todorovic, L., Silva, V., 2022. A liquefaction occurrence model for regional analysis. *Soil Dyn. Earthq.* 161, 107430.
- Tokimatsu, K., Tamura, S., Suzuki, H., Katsumata, K., 2012. Building damage associated with geotechnical problems in the 2011 Tohoku Pacific Earthquake. *Soils Found.* 52 (5), 956–974.
- Totschnig, R., Fuchs, S., 2013. Mountain torrents: quantifying vulnerability and assessing uncertainties. *Eng. Geol.* 155, 31–44.
- Ujjwal, K.C., Garg, S., Hilton, J., Aryal, J., 2020. A cloud-based framework for sensitivity analysis of natural hazard models. *Environ. Model. Softw.* 134, 104800.
- UNDRR, 2015. Global Assessment Report on Disaster Risk Reduction 2015. United Nations Office for Disaster Risk Reduction.
- Van Ballegooij, S., Malan, P., Lacrosse, V., Jacka, M.E., Cubrinovski, M., Bray, J.D., O'Rourke, T.D., Crawford, S.A., Cowan, H., 2014. Assessment of liquefaction-induced land damage for residential Christchurch. *Earthquake Spectra* 30 (1), 31–55.
- Wald, D.J., Allen, T.L., 2007. Topographic slope as a proxy for seismic site conditions and amplification. *Bull. Seismol. Soc. Am.* 97 (5), 1379–1395.
- Worden, C.B., Thompson, E.M., Hearne, M., Wald, D.J., 2020. ShakeMap Manual Online: Technical Manual, User's Guide, and Software Guide. US Geological Survey.
- Youd, T.L., Perkins, D.M., 1978. Mapping liquefaction-induced ground failure potential. *J. Geotech. Eng. Div.* 104 (4), 433–446.
- Zhu, J., Daley, D., Baise, L.G., Thompson, E.M., Wald, D.J., Knudsen, K.L., 2015. A geospatial liquefaction model for rapid response and loss estimation. *Earthquake Spectra* 31 (3), 1813–1837.
- Zhu, J., Baise, L.G., Thompson, E.M., 2017. An updated geospatial liquefaction model for global application. *Bull. Seismol. Soc. Am.* 107, 1365–1385.